Supplement of Atmos. Chem. Phys., 23, 6431–6456, 2023
https://doi.org/10.5194/acp-23-6431-2023-supplement

Atmospheric Chemistry and Physics
Open Access
EGU

Supplement of

Ambient carbonaceous aerosol levels in Cyprus and the role of pollution transport from the Middle East

Aliki Christodoulou et al.

Correspondence to: Aliki Christodoulou (a.christodoulou@cyi.ac.cy) and Jean Sciare (j.sciare@cyi.ac.cy)

Section S1. PMF methodology

Initially, the reference factor profile (RFP) BBOA from Ng et al., 2011 was used to constrain the PMF. The m/z 60 cannot be explained by any combination of a-values (constrained). The combinations presented in Table S1 have been used and resulted in non-optimum correlations between BC_{wb} vs BBOA. The correlation of BCwb with the other factor that contained m/z 60 was better with an R^2 up to 0.84.

Table S1: Changes in correlation coefficient of BC_{ff} vs HOA-1 and BC_{wb} and BC_{wb} vs BBOA for different a-values used to constrained the BBOA mass spectrum.

a-value	r^2 of BC_{ff} vs HOA-1	r^2 of BC_{wb} vs BBOA
0.3	0.53	0.66
0.35	0.54	0.26
0.4	0.56	0.01
0.45	0.56	0.02

The second step was to search for a local BBOA factor. The unconstrained solutions have shown very good correlation for BBOA vs BC_{wb}. Thus, the unconstrained runs have been used to calculate the local BBOA reference factor. Both 4-factor and 5-factor solution runs were tested. For the 4-factor solution, the HOA factor retrieved had a clear pattern containing the alkane and alkene related fragments and wasn't containing m/z 44. BBOA factor retrieved was containing 99% of the m/z 60 included in the dataset. The 5-factor solution of unconstrained PMF runs exhibits a separation between primary and secondary factors, however the solution among the runs isn't that stable. Critically, the BBOA profile factor wasn't as stable as in the 4-factor solution (Fig. S1).

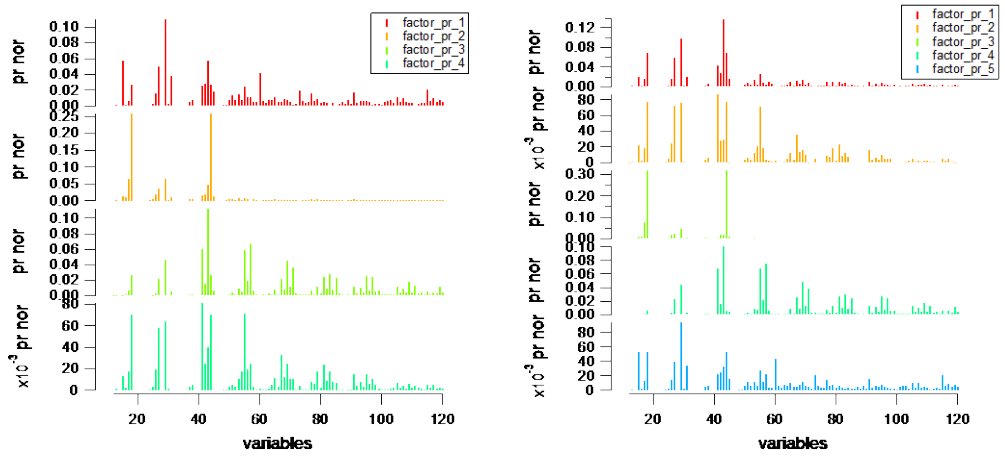

(a) (b)

Figure S1. Factor profiles for the four- (a) and five- (b) factor unconstrained runs for the 2017 cold period dataset.

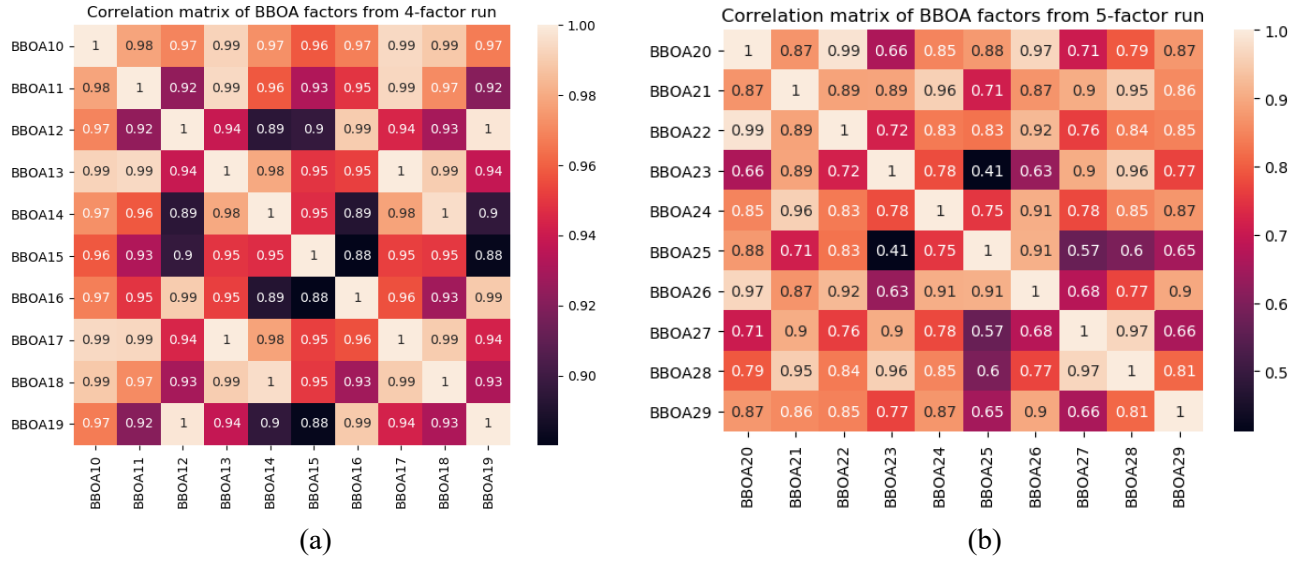

Figure S2. Coefficient of determination for linear regression (r^2) of deconvolved BBOA profiles from the 4-factor unconstrained run (a) and 5-factor unconstrained run (b).

25

As observed in Fig. S2, the 4-factor solution was having quite similar factor profiles for BBOA compared to the 5-factor unconstrained runs. Thus, the 4-factor solution has been used to derive this BBOA-like local factor in Nicosia ($BBOA_{cy}$ more effectively. In the figure S3 the mass spectra of the calculated $BBOA_{cy}$ is presented.

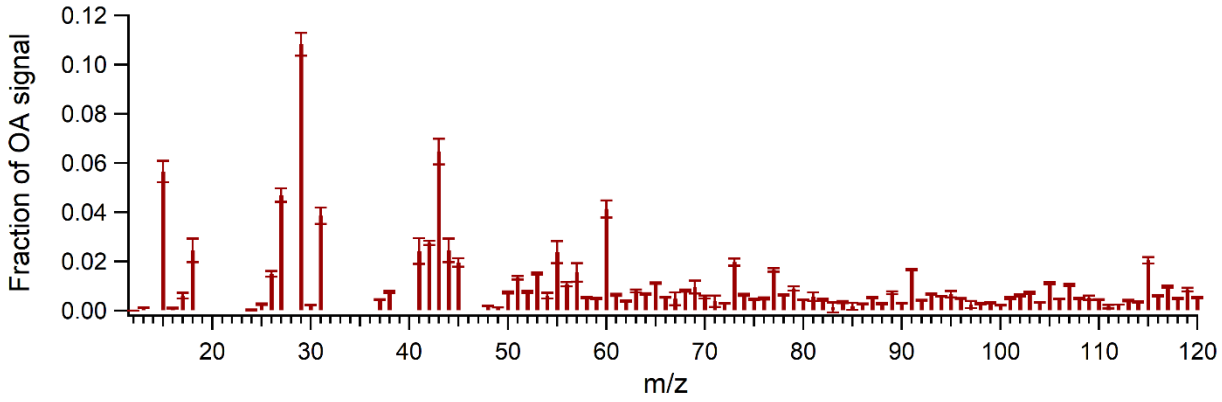

30 **Figure S3: The mass spectra of the calculated $BBOA_{cy}$ averaging the unconstrained solutions. Error bars represent one standard deviation of the averaged unconstrained solutions.**

Applying a-values (0-0.5 with a step of 0.02) for the $BBOA_{CY}$ revealed that the best solution was to use an a-value of 0.46. It was the most stable solution among all, having good correlation of BBOA factor with BC_{wb} (r^2 = 0.84), and HOA factor with BC_{ff} (r^2 = 0.67). Additionally, the a-value of 0.46 also had the most stable factor profile results.

Afterwards, the optimum a-value for HOA was selected. To do so, the $BBOA_{CY}$ factor was anchored with an a-value of 0.46 and a first-dimension sensitivity analysis for the HOA-like reference factor from Ng et al., (2011) was used with a-values ranging from 0 to 0.2 with a step of 0.02. All a–values ranging 0.1 to 0.2 resulted in similar correlation between HOA factors and BC_{ff} ($r^2 = 0.65$). However, the contribution of HOA factor increased as the a-value was increased. Finally, the a-value of 0.2 was selected so that maximum freedom was given to the system to explain all possible emissions from fossil fuel combustion.

Section S2. Supplementary Figures/Tables

Table S2: ACSMs sampling setup at Nicosia site for the 6-month measuring period.

	Value
RF$_{NO_3}$	4.78 *10-11
RIE$_{NH_4}$	5.2
RIE$_{SO_4}$	0.51
RIE$_{Cl}$	1.3

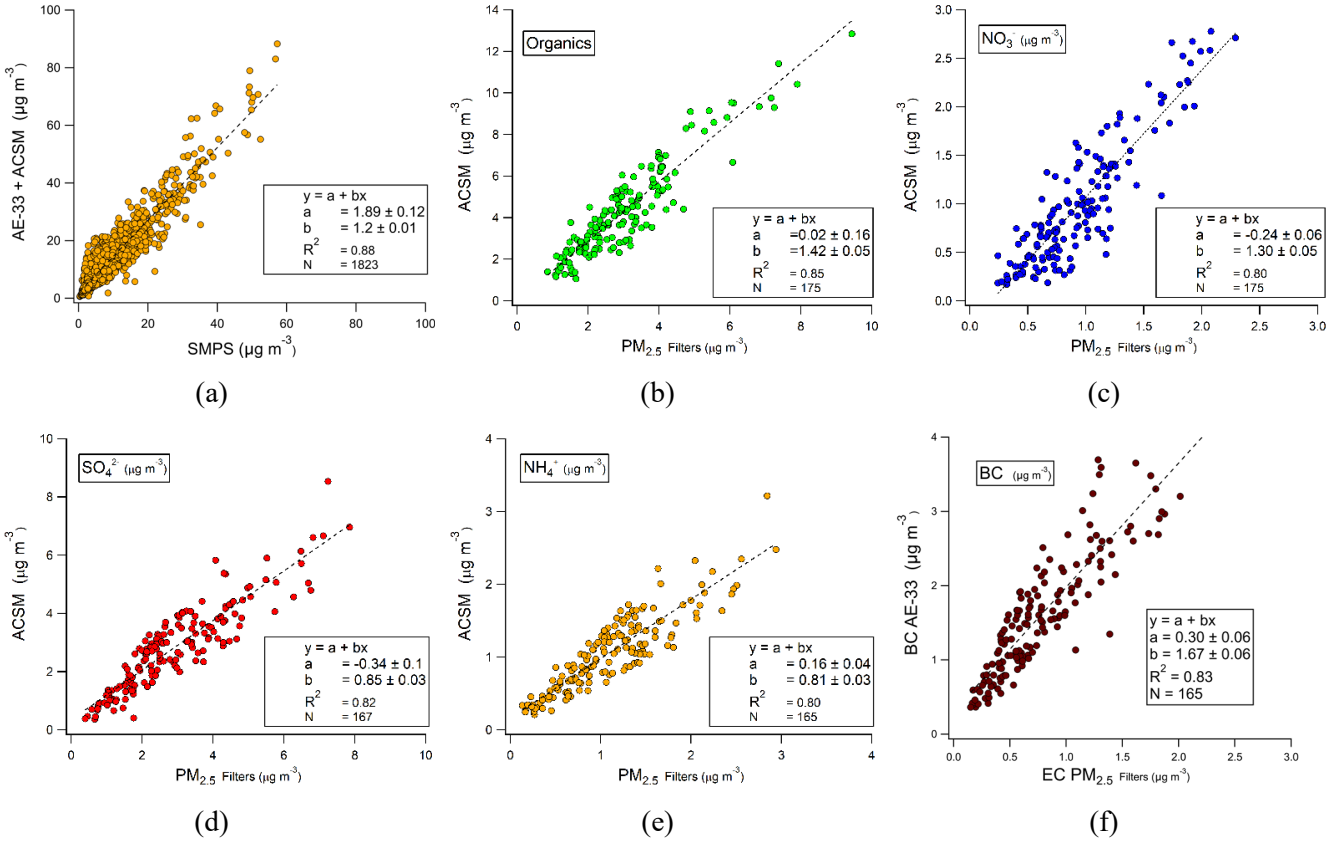

Figure S4: a) Mass closure exercise between daily averaged reconstructed PM$_1$ (ACSM+BC) and measured PM$_1$ by SMPS. b-e) Scatterplot of chemically speciated ACSM measurements versus filter analyses for organic matter (compared to OC filter- based measurements), nitrate, sulfate and ammonium. f) Comparison of daily average BC and EC concentrations.

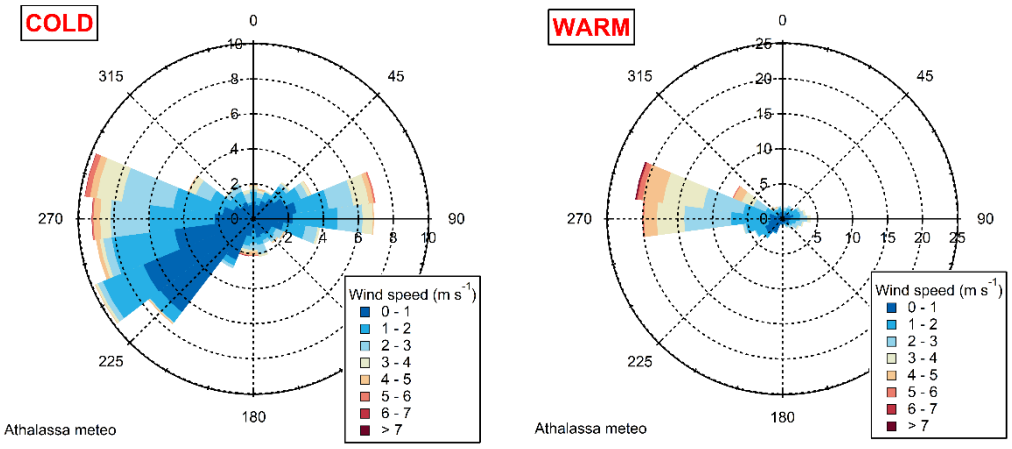

(a) (b)

Figure S5. Wind roses for (a) the cold season and (b) the warm season respectively. Wind direction and velocity data obtained by the Athalassa Forestry Park Meteorological Station operated by the Cyprus Department of Meteorology.

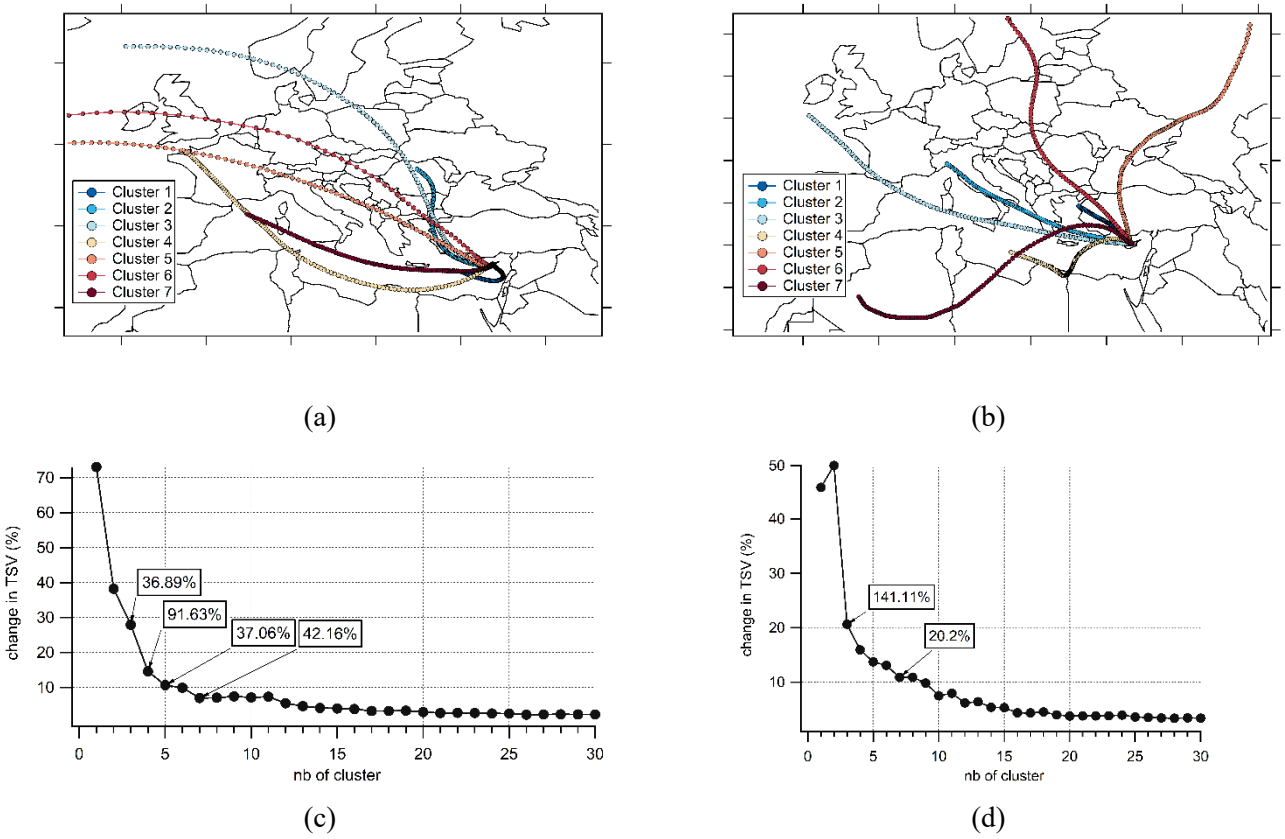

(a) (b)

(c) (d)

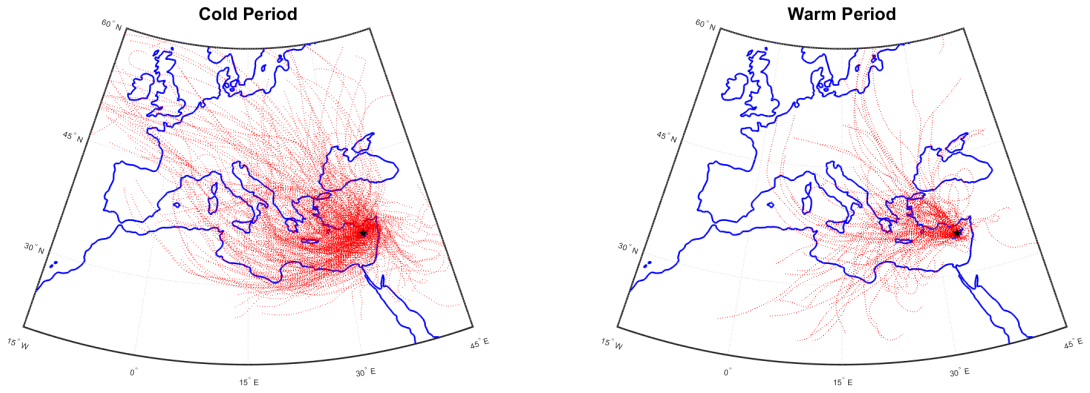

(e) (f)

Figure S6: Cluster analysis for backward trajectories of air masses during the cold (a) and warm (b) period. Percentage change in Total Spatial Variance as a function of the number of clusters for the (c) cold and (d) warm periods. Calculated 72h back trajectories arriving at the measuring site every 6 hours for both the cold (e) and warm (f) periods.

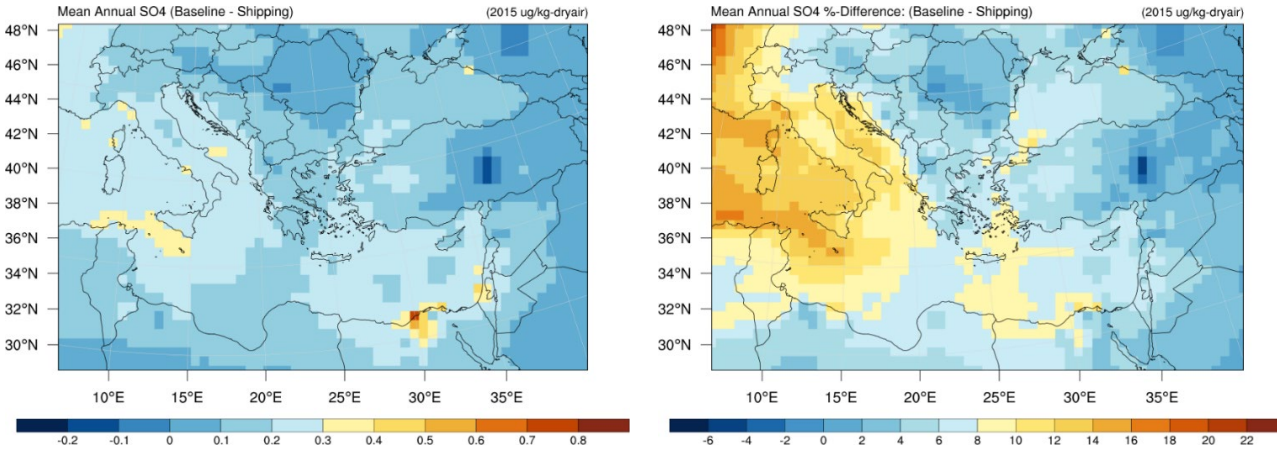

(a) **(b)**

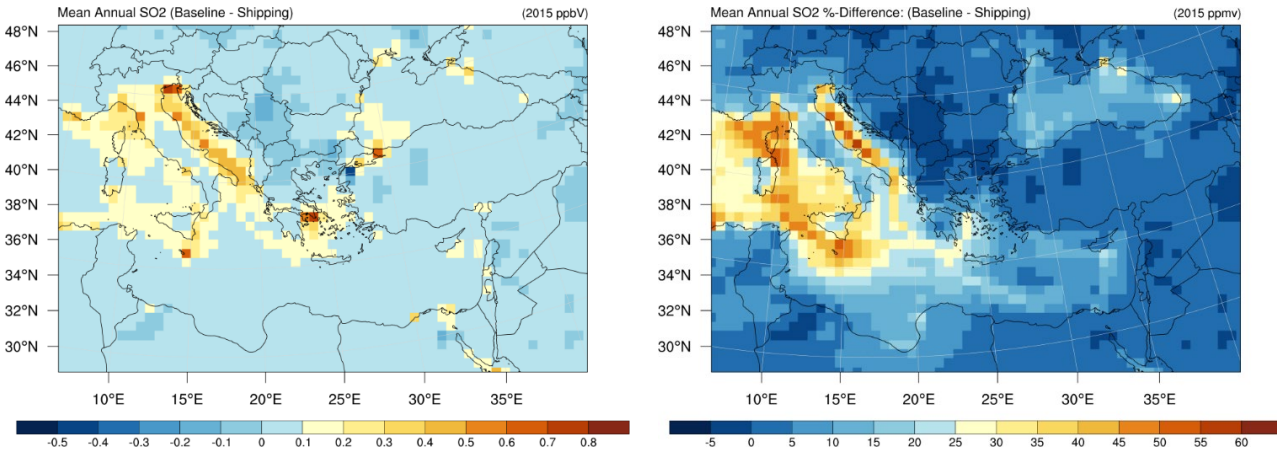

(c) **(d)**

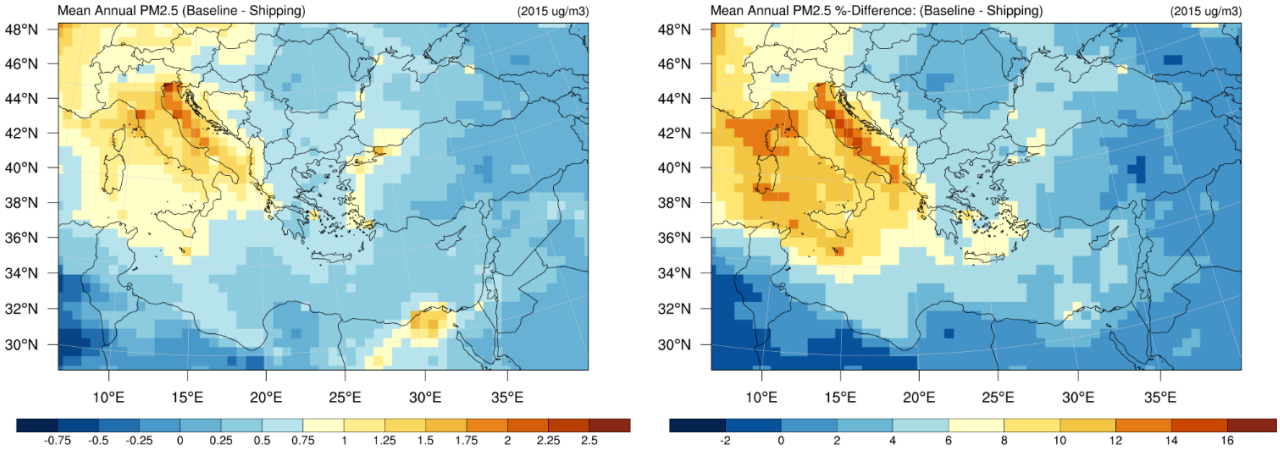

(e) **(f)**

Figure S7: Difference in mean annual modelled surface concentrations of (a, b) $SO_4^=$, (c, d) SO_2 and (e, f) $PM_{2.5}$ in absolute values (a, c, e) and percentage (b, d, f) between the baseline S0 and no-shipping emissions S1 simulations.

60

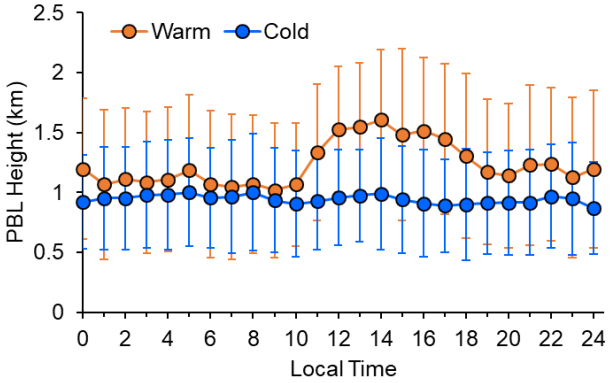

Figure S8: Diurnal profile of the planetary boundary layer height calculated by the LIDAR measurements for both periods in Nicosia.

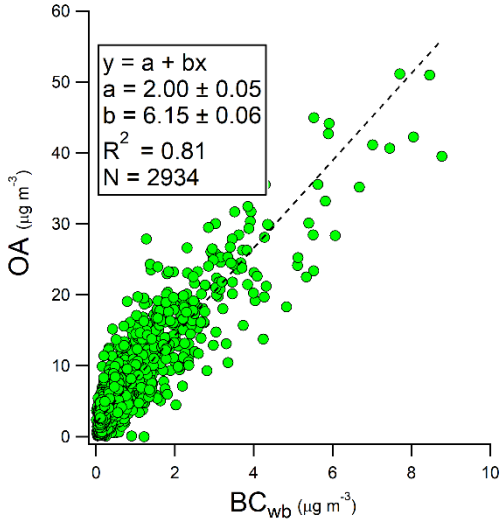

Figure S9: Scatter plot and linear regression of OA measured in Nicosia during the cold period versus BC_{wb} obtained by the aethalometer model.

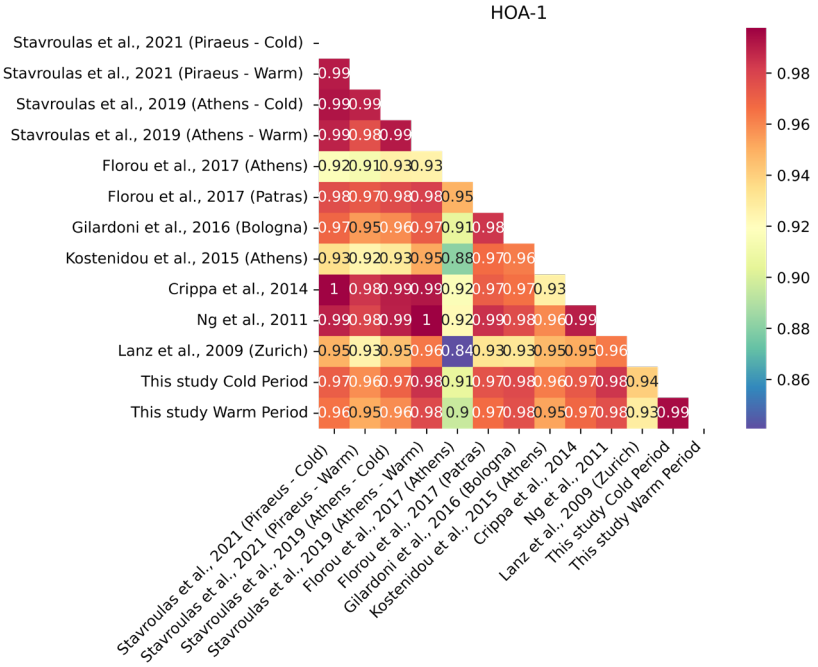
HOA-1
Stavroulas et al., 2021 (Piraeus - Cold)
Stavroulas et al., 2021 (Piraeus - Warm)
Stavroulas et al., 2019 (Athens - Cold)
Stavroulas et al., 2019 (Athens - Warm)
Florou et al., 2017 (Athens)
Florou et al., 2017 (Patras)
Gilardoni et al., 2016 (Bologna)
Kostenidou et al., 2015 (Athens)
Crippa et al., 2014
Ng et al., 2011
Lanz et al., 2009 (Zurich)
This study Cold Period
This study Warm Period
0.98
0.96
0.94
0.92
0.90
0.88
0.86

(a)

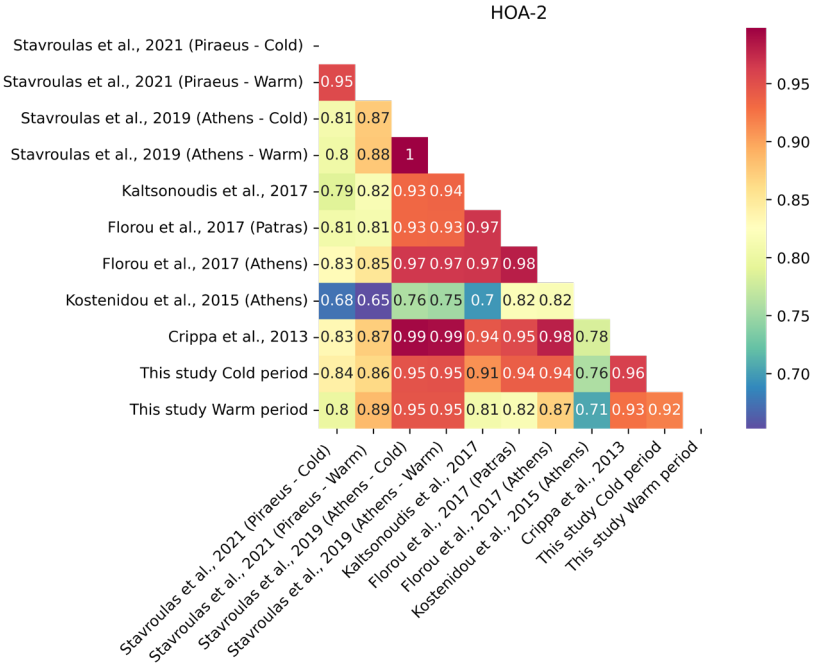
HOA-2
Stavroulas et al., 2021 (Piraeus - Cold)
Stavroulas et al., 2021 (Piraeus - Warm)
Stavroulas et al., 2019 (Athens - Cold)
Stavroulas et al., 2019 (Athens - Warm)
Kaltsonoudis et al., 2017
Florou et al., 2017 (Patras)
Florou et al., 2017 (Athens)
Kostenidou et al., 2015 (Athens)
Crippa et al., 2013
This study Cold period
This study Warm period
0.95
0.90
0.85
0.80
0.75
0.70

(b)

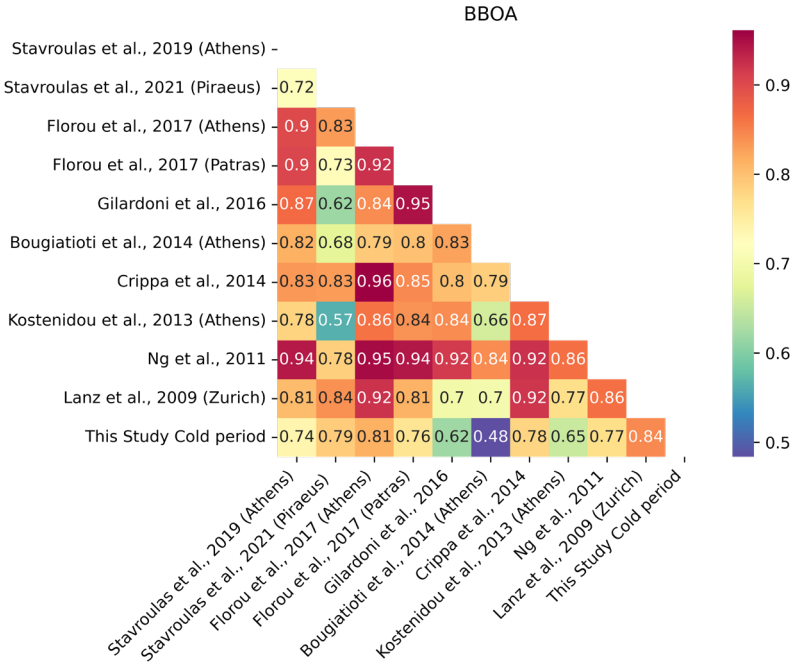
BBOA
Stavroulas et al., 2019 (Athens)
Stavroulas et al., 2021 (Piraeus)
Florou et al., 2017 (Athens)
Florou et al., 2017 (Patras)
Gilardoni et al., 2016
Bougiatioti et al., 2014 (Athens)
Crippa et al., 2014
Kostenidou et al., 2013 (Athens)
Ng et al., 2011
Lanz et al., 2009 (Zurich)
This Study Cold period
0.9
0.8
0.7
0.6
0.5

(c)

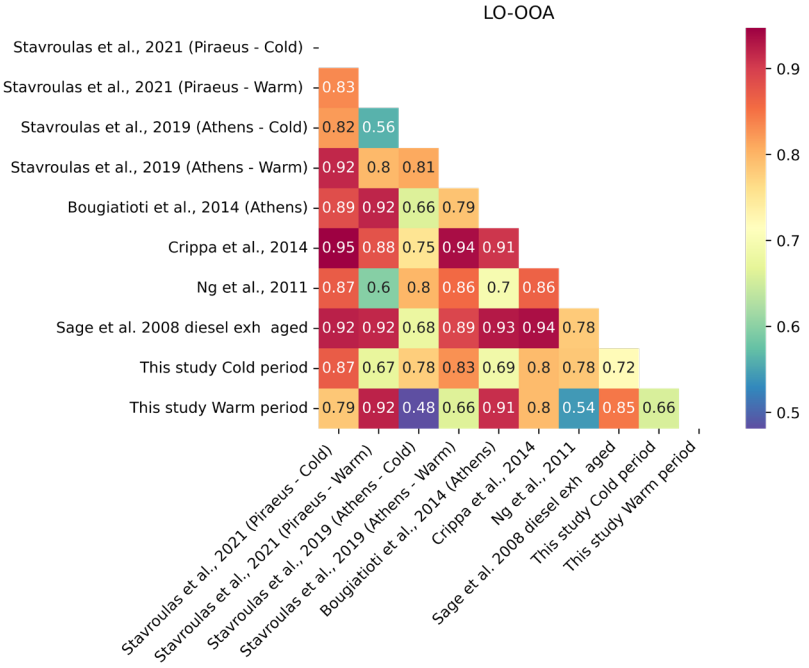
LO-OOA
Stavroulas et al., 2021 (Piraeus - Cold)
Stavroulas et al., 2021 (Piraeus - Warm)
Stavroulas et al., 2019 (Athens - Cold)
Stavroulas et al., 2019 (Athens - Warm)
Bougiatioti et al., 2014 (Athens)
Crippa et al., 2014
Ng et al., 2011
Sage et al. 2008 diesel exh aged
This study Cold period
This study Warm period
0.9
0.8
0.7
0.6
0.5

(d)

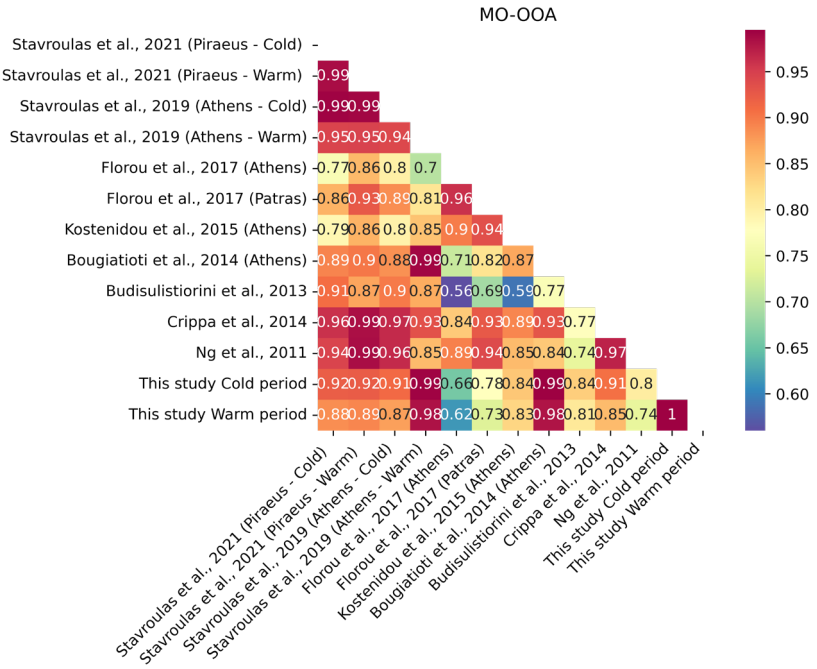

(e)

Figure S10: Correlation matrices of resolved OA factor profiles against selected factor profiles found in the literature. Note that the m/z 18, 28 were excluded from the comparison to literature mass spectra.

70

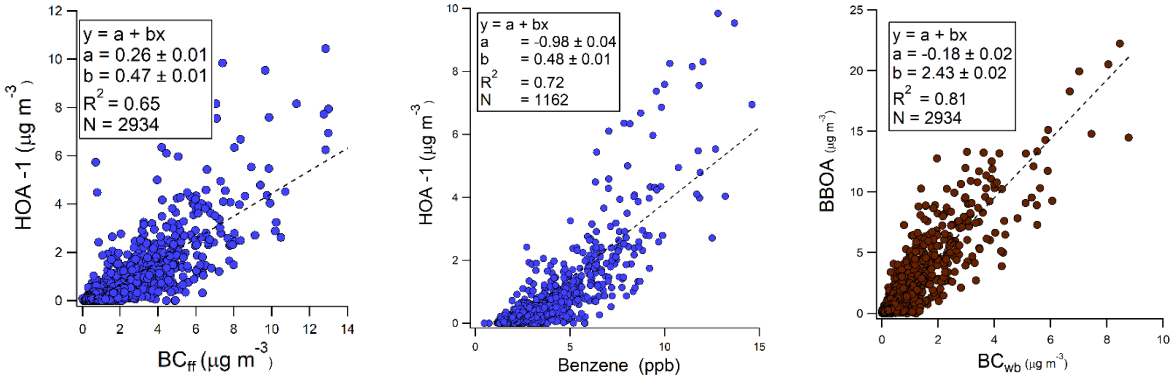

(a) (b) (c)

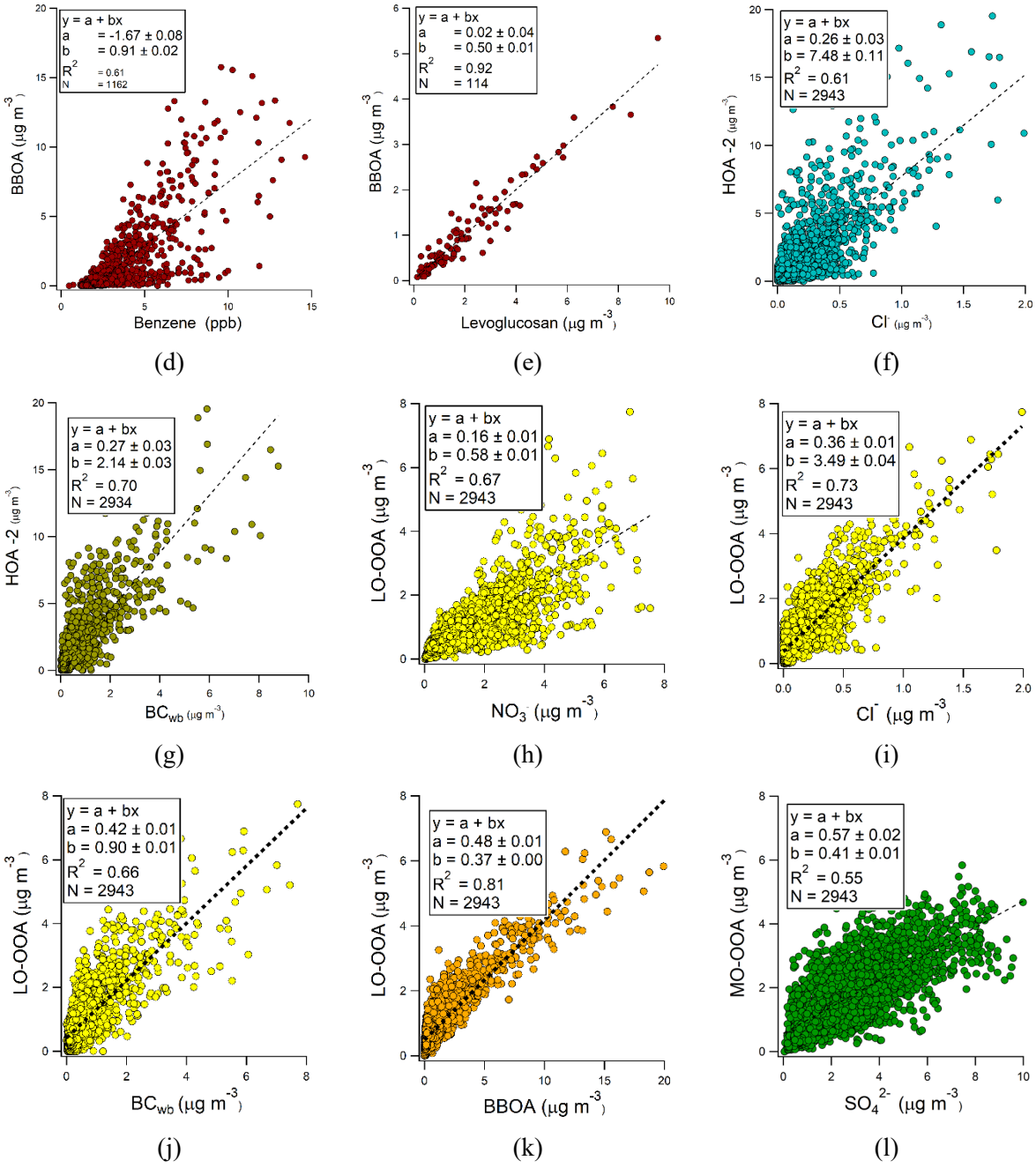

Figure S11: Comparison of OA factor time series with external tracers during the cold period

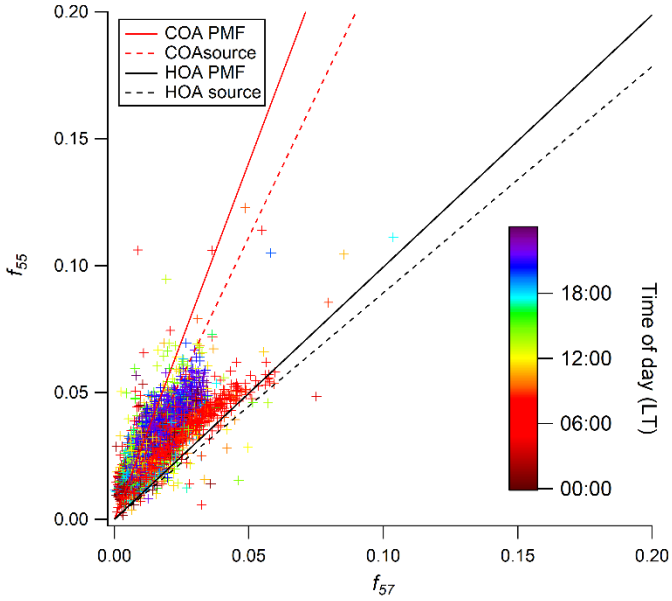

Figure S12: Mass fraction of m/z 55 and 57 (f 55 and f 57) for primary organics. F 55 and F 57 linear fits extracted from various PMF COA and HOA factors (red and black line accordingly), as well as from cooking and traffic source emission studies (red and black dashed line accordingly) reported in (Mohr et al., 2012). Data points are coloured according to time of day.

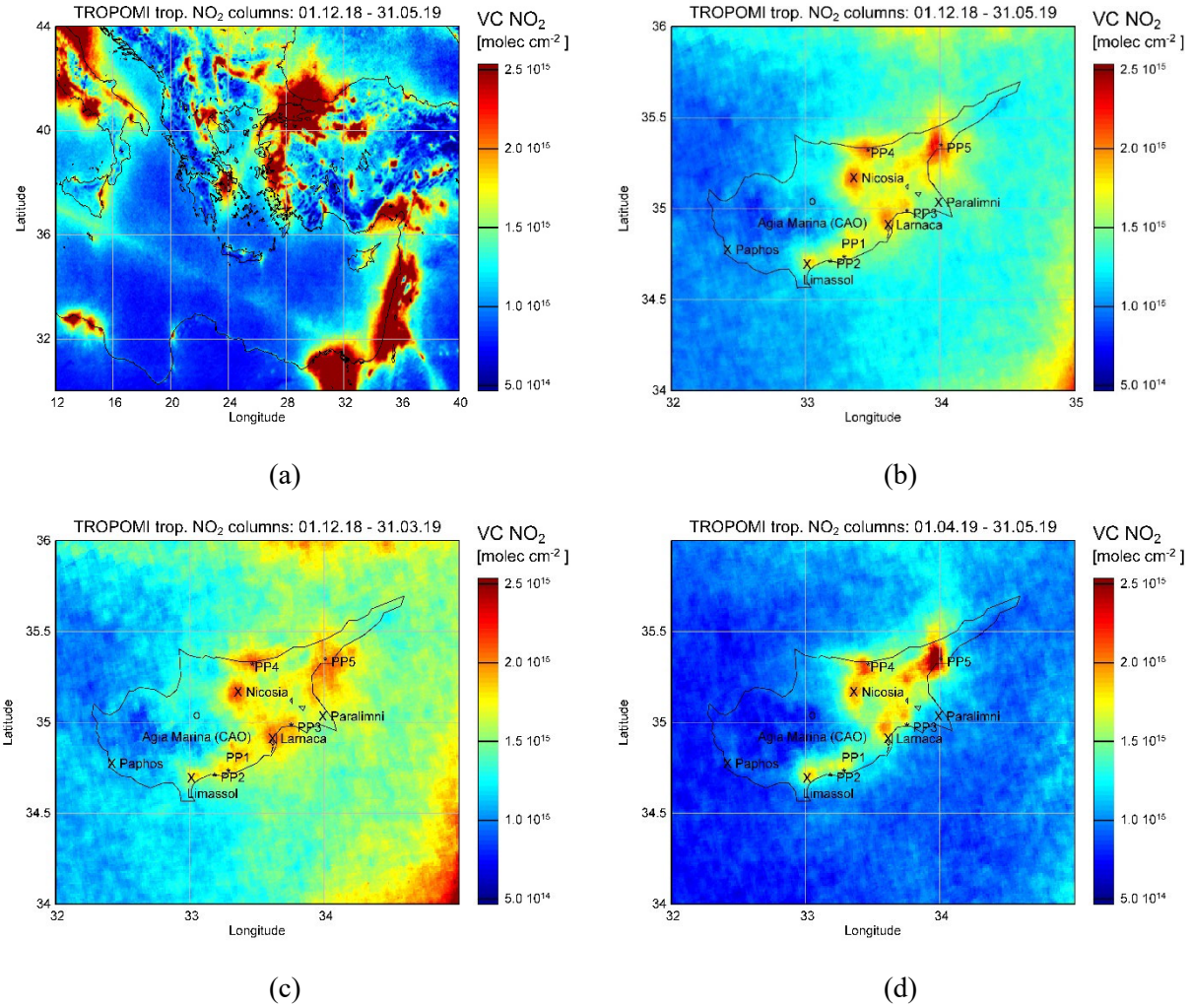

Figure S13: Spatial variability of space-based (SP5-TROPOMI) vertical columns of NO_2 in the East Mediterranean (a) and Cyprus (b) for the entire period of the campaign. Cold and warm period (c and d) with the geolocation of the main urban centers and power plants in Cyprus and the location of the background station CAO (x Nicosia).

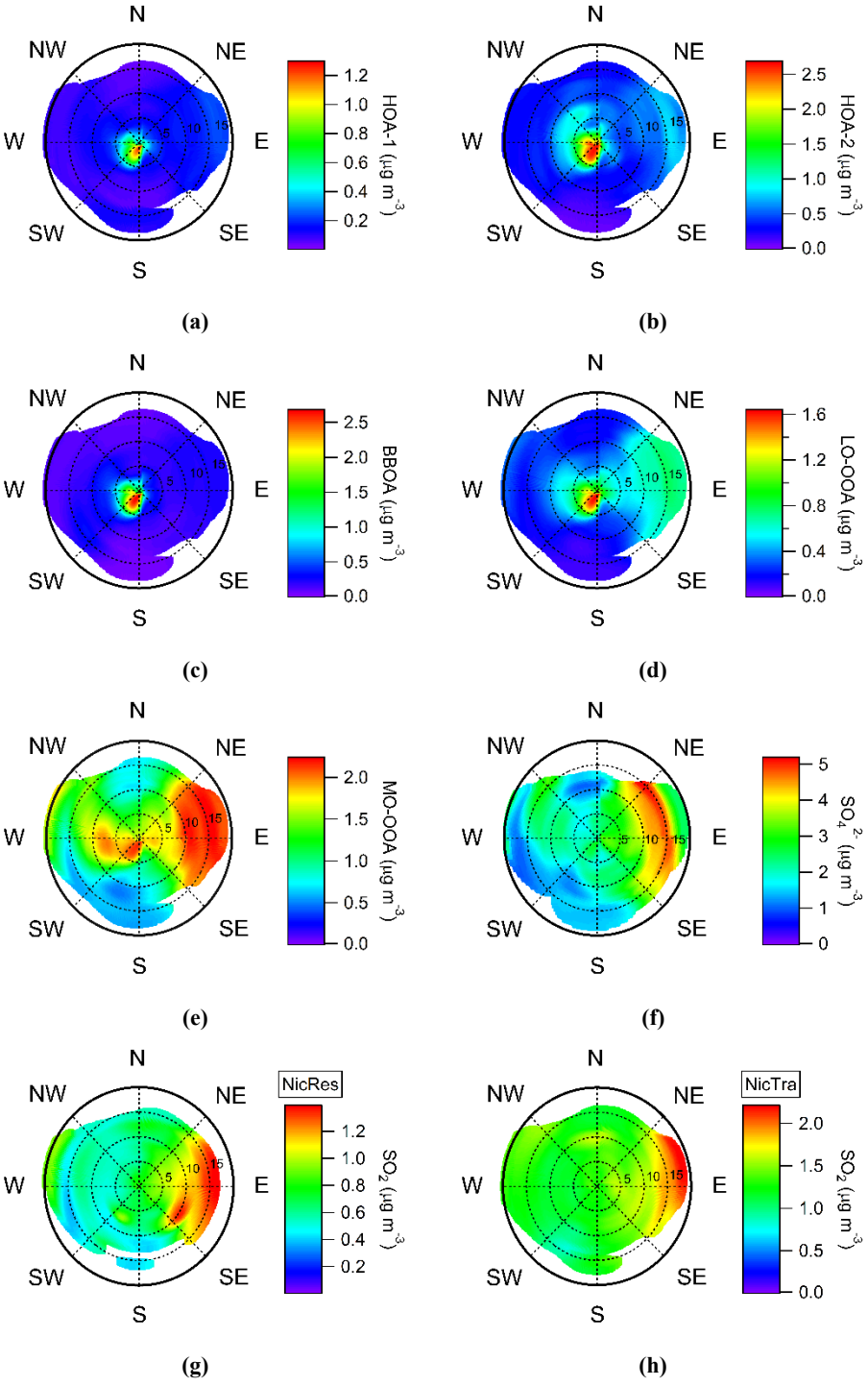
N
NW
NE
W
E
SW
SE
S
5
10
15
HOA-1 (μg m-3)
1.2
1.0
0.8
0.6
0.4
0.2
(a)
HOA-2 (μg m-3)
2.5
2.0
1.5
1.0
0.5
0.0
(b)
BBOA (μg m-3)
(c)
LO-OOA (μg m-3)
1.6
1.2
0.8
0.4
(d)
MO-OOA (μg m-3)
(e)
SO4 2- (μg m-3)
5
4
3
2
1
0
(f)
NicRes
SO2 (μg m-3)
(g)
NicTra
(h)

Figure S14: Non-Parametric Wind (NWR) regression polar plots for (a) HOA-1, (b) HOA-2, (c) BBOA, (d)LO – OOA and (e) MO – OOA, calculated for the cold period in Nicosia. Non-Parametric Wind (NWR) regression polar plots calculated for f) SO_4^{2-} at the CAO-NIC (g) SO_2 at the residential and (h) SO_2 at the traffic site, for the cold period in Nicosia.

90

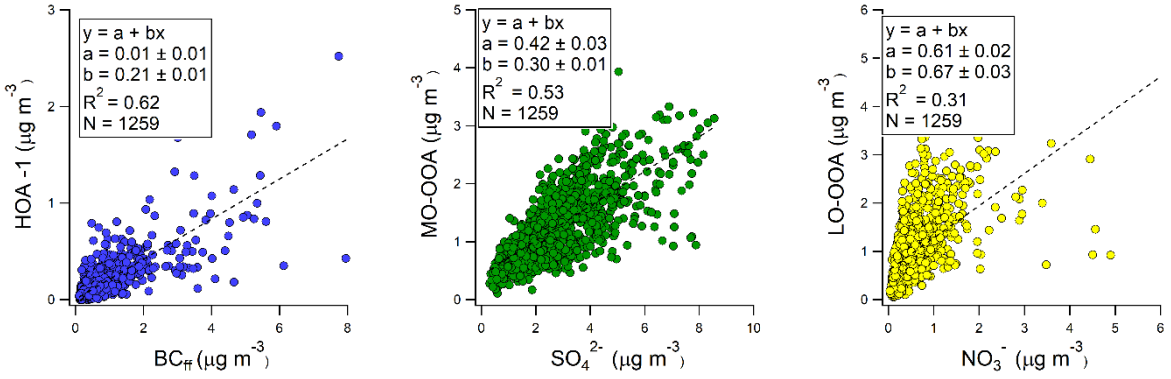

(a) (b) (c)

Figure S15 Comparison of OA factor timeseries with external tracers during the warm period

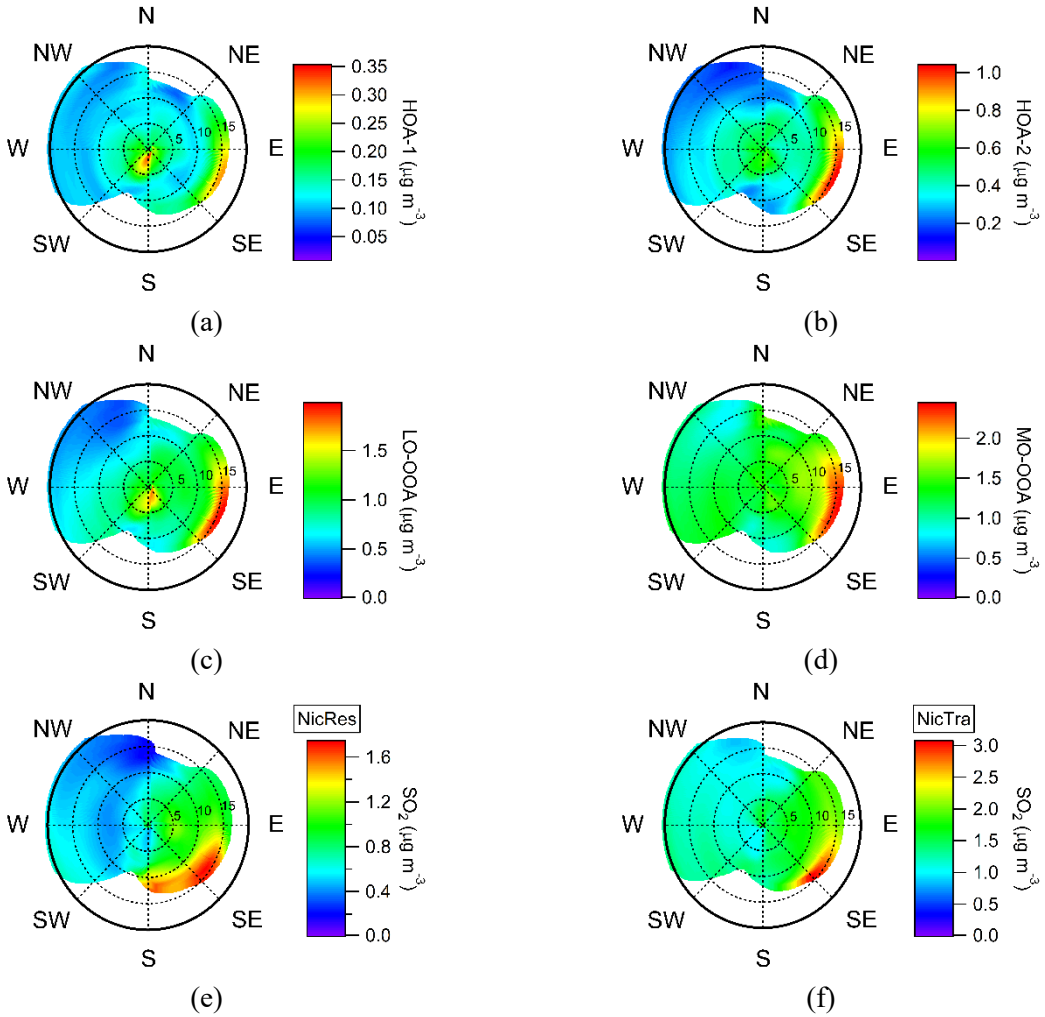

Figure S16: Non-Parametric Wind (NWR) regression polar plots for (a) HOA-1, (b) HOA-2, (c) LO – OOA and (d) MO – OOA, calculated for the warm period in Nicosia. Non-Parametric Wind (NWR) regression polar plots calculated for (e) SO2 at the residential and (f) SO2 at the traffic site, for the warm period in Nicosia.

Table S3: OA factor sources mean, standard deviation, median concentrations and respective contribution to total OA during cold and warm periods in Nicosia.

	Cold Period				Warm Period			
μg m^{-1}	**Mean**	**Std**	**Median**	**Contribution (%)**	**Mean**	**Std**	**Median**	**Contribution (%)**
HOA - 1	0.46	0.93	0.17	7	0.17	1.91	0.11	6
BBOA	1.01	2.15	0.25	12	-	-	-	-
HOA - 2	1.33	2.07	0.61	21	0.45	0.56	0.34	16
MO - OOA	1.75	1.06	1.60	44	1.27	0.55	1.19	45
LO - OOA	0.86	0.88	0.58	16	0.95	0.11	0.60	34

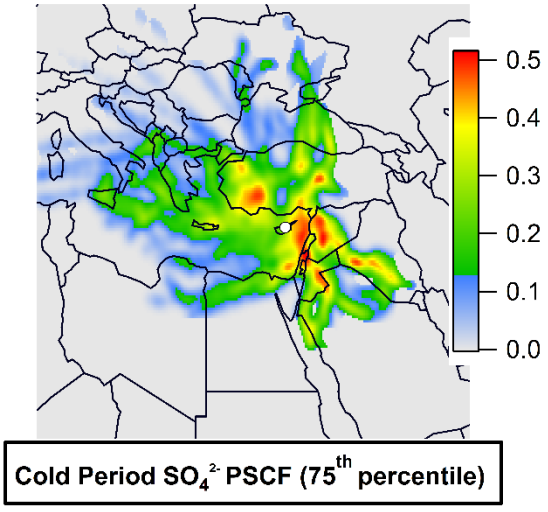

(a)

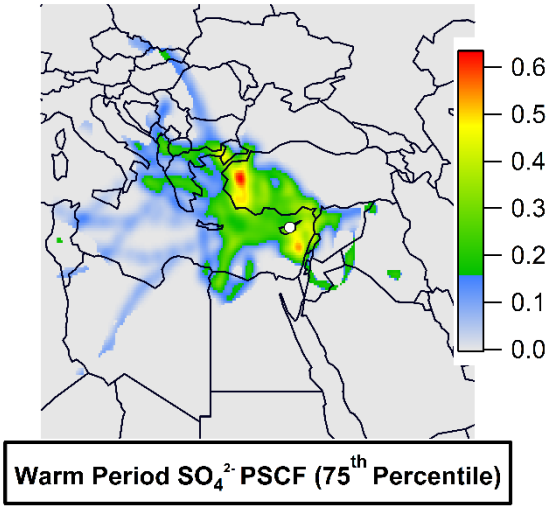

(b)

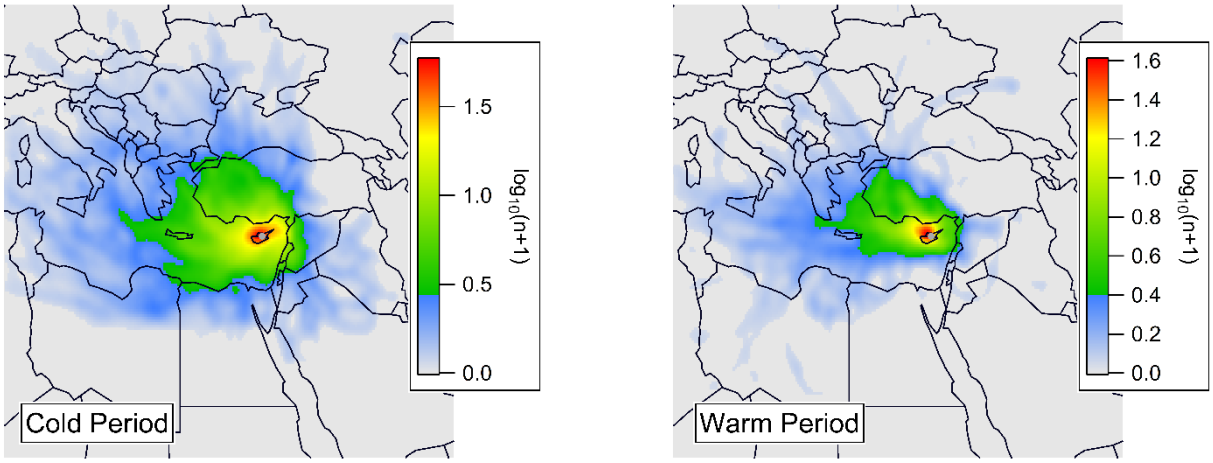

(c) (d)

Figure S17: PSCF calculated for the 75th percentile for SO_4^{2-} for the (a) cold and (b) warm period respectively. Log10(n+1) trajectory density plots for both the (c) cold and (d) warm periods.

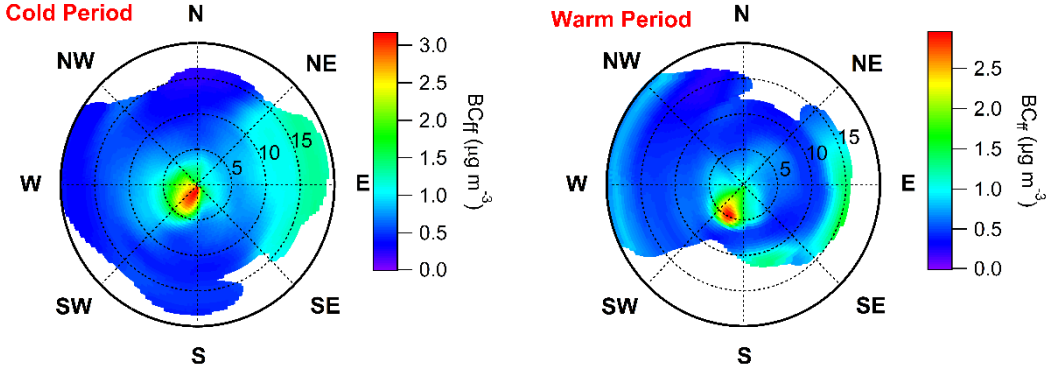

(a) (b)

Figure S18. Non-Parametric Wind regression (NWR) polar plots calculated for BC_{ff} during the (a) cold and (b) warm period in Nicosia.

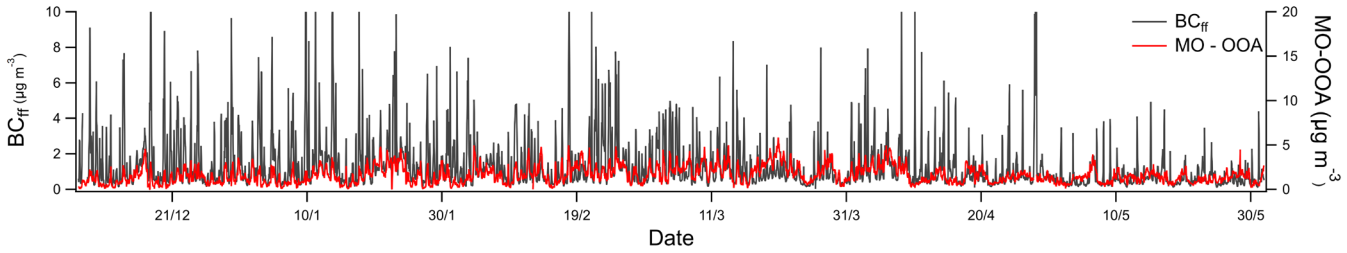

Figure S19: Temporal variability of BC_{ff} and MO-OOA concentrations during the entire measuring period.

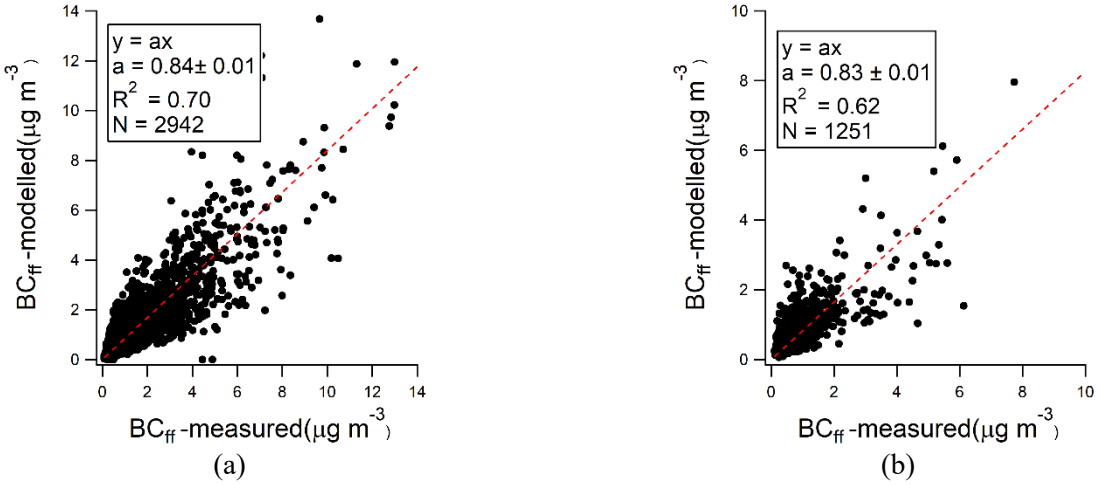

Figure S20: Correlation between measured and modelled BCff for the cold (a) and warm (b) period. The correlation curve (red lines) were calculated using the least orthogonal distance fit method.

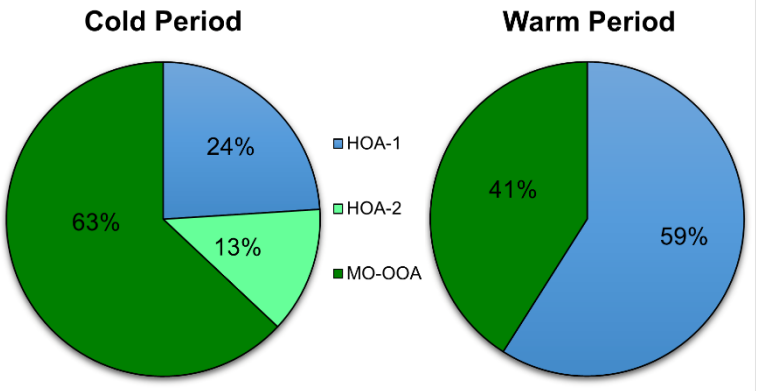

Figure S21: BC_{ff} contributions related to the sources retrieved from OA source apportionment for the cold (left) and warm (right) period.

Section S3. Aethalometer model

For the selection of the optimum AAE values for the aethalometer model a sensitivity analysis was performed. In this context, the aethalometer model was implemented using all the different combinations with a_{ff} varying between 0.8 and 1.2 with an increment of 0.05 and a_{wb} varying from 1.4 through 2.4 with an increment of 0.1. Linear regression was consequently performed between BC_{wb} and the OA concentration at m/z = 60, a fragment directly linked to levoglucosan, thus used as a biomass-burning tracer. Furthermore, linear regression of BC_{ff} vs xylenes (C_8H_{11}) was also performed for the cold period, when VOC measurements were available.

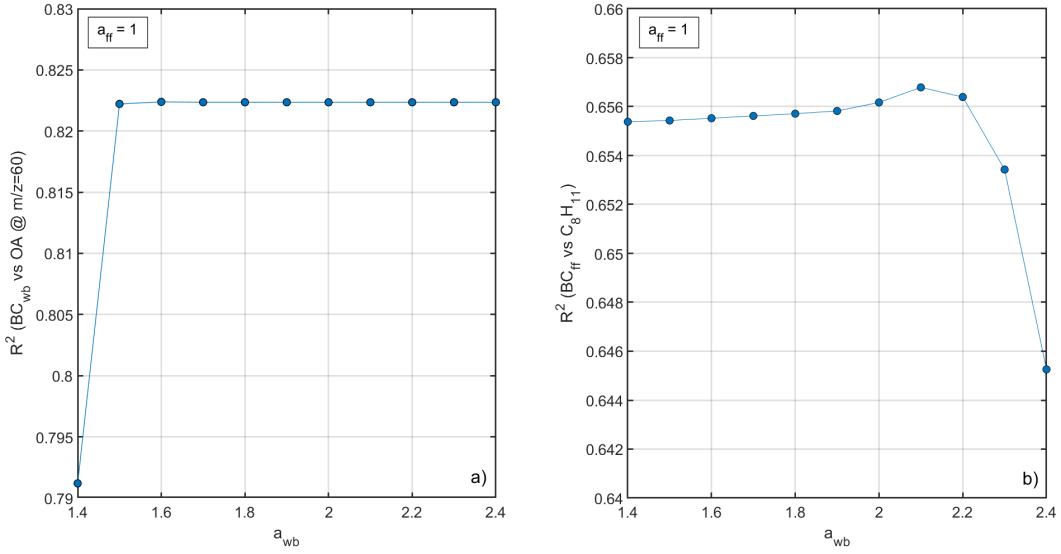

Figure S22: Squared Pearson correlation coefficient (R^2) for the linear regression of (a) BC_{wb} versus OA at m/z=60 and BC_{ff} versus xylenes, keeping an a_{ff} value of 1 and varying a_{wb}.

As depicted in Fig. 3 when keeping an a_{ff} value of 1, no change has been observed for the correlation of BC_{wb} to OA at m/z=60 with varying values for a_{wb}, with R^2 being 0.822 constantly for a_{wb} above 1.5. For the same scenario, a rather insignificant increase in R^2 values was observed for the correlation of BC_{ff} to xylenes when moving from a_{wb}=2 to a_{wb}=2.1.

Finally, the correlation between daily averaged BC_{wb} values and concurrent levoglucosan concentrations, a well-established biomass burning tracer, obtained through filter sampling, is excellent (R^2 = 0.94) when using the "default" AAE values (a_{ff}=1 and a_{wb}=2). Thus, the selection of these values for the Aethalometer model, seems to provide results that capture the residential wood burning phenomenon in a quite satisfactory manner for the urban background conditions in Nicosia.

References

Bougiatioti, A., Stavroulas, I., Kostenidou, E., Zarmpas, P., Theodosi, C., Kouvarakis, G., Canonaco, F., Prévôt, A. S. H., Nenes, A., Pandis, S. N., and Mihalopoulos, N.: Processing of biomass-burning aerosol in the eastern Mediterranean during summertime, Atmos. Chem. Phys., https://doi.org/10.5194/acp-14-4793-2014, 2014.

Budisulistiorini, S. H., Canagaratna, M. R., Croteau, P. L., Marth, W. J., Baumann, K., Edgerton, E. S., Shaw, S. L., Knipping, E. M., Worsnop, D. R., Jayne, J. T., Gold, A., and Surratt, J. D.: Real-time continuous characterization of secondary organic aerosol derived from isoprene epoxydiols in downtown Atlanta, Georgia, using the aerodyne aerosol chemical speciation monitor, Environ. Sci. Technol., 47, 5686–5694, https://doi.org/10.1021/es400023n, 2013.

Crippa, M., Decarlo, P. F., Slowik, J. G., Mohr, C., Heringa, M. F., Chirico, R., Poulain, L., Freutel, F., Sciare, J., Cozic, J., Di Marco, C. F., Elsasser, M., Nicolas, J. B., Marchand, N., Abidi, E., Wiedensohler, A., Drewnick, F., Schneider, J., Borrmann, S., Nemitz, E., Zimmermann, R., Jaffrezo, J. L., Prévôt, A. S. H., and Baltensperger, U.: Wintertime aerosol chemical composition and source apportionment of the organic fraction in the metropolitan area of Paris, Atmos. Chem. Phys., 13, 961–981, https://doi.org/10.5194/acp-13-961-2013, 2013.

Crippa, M., Canonaco, F., Lanz, V. A., Äijälä, M., Allan, J. D., Carbone, S., Capes, G., Ceburnis, D., Dall'Osto, M., Day, D. A., DeCarlo, P. F., Ehn, M., Eriksson, A., Freney, E., Ruiz, L. H., Hillamo, R., Jimenez, J. L., Junninen, H., Kiendler-Scharr, A., Kortelainen, A. M., Kulmala, M., Laaksonen, A., Mensah, A. A., Mohr, C., Nemitz, E., O'Dowd, C., Ovadnevaite, J., Pandis, S. N., Petäjä, T., Poulain, L., Saarikoski, S., Sellegri, K., Swietlicki, E., Tiitta, P., Worsnop, D. R., Baltensperger, U., and Prévôt, A. S. H.: Organic aerosol components derived from 25 AMS data sets across Europe using a consistent ME-2 based source apportionment approach, Atmos. Chem. Phys., 14, 6159–6176, https://doi.org/10.5194/acp-14-6159-2014, 2014.

Florou, K., Papanastasiou, D. K., Pikridas, M., Kaltsonoudis, C., Louvaris, E., Gkatzelis, G. I., Patoulias, D., Mihalopoulos, N., and Pandis, S. N.: The contribution of wood burning and other pollution sources to wintertime organic aerosol levels in two Greek cities, Atmos. Chem. Phys., 17, 3145–3163, https://doi.org/10.5194/acp-17-3145-2017, 2017.

Gilardoni, S., Massoli, P., Paglione, M., Giulianelli, L., Carbone, C., Rinaldi, M., Decesari, S., Sandrini, S., Costabile, F., Gobbi, G. P., Pietrogrande, M. C., Visentin, M., Scotto, F., Fuzzi, S., and Facchini, M. C.: Direct observation of aqueous secondary organic aerosol from biomass-burning emissions, Proc. Natl. Acad. Sci. U. S. A., 113, 10013–10018, https://doi.org/10.1073/pnas.1602212113, 2016.

Kaltsonoudis, C., Kostenidou, E., Louvaris, E., Psichoudaki, M., Tsiligiannis, E., Florou, K., Liangou, A., and Pandis, S. N.: Characterization of fresh and aged organic aerosol emissions from meat charbroiling, Atmos. Chem. Phys., 17, 7143–7155,

https://doi.org/10.5194/acp-17-7143-2017, 2017.

Kostenidou, E., Florou, K., Kaltsonoudis, C., Tsiflikiotou, M., Vratolis, S., Eleftheriadis, K., and Pandis, S. N.: Sources and chemical characterization of organic aerosol during the summer in the eastern Mediterranean, Atmos. Chem. Phys., 15, 11355–11371, https://doi.org/10.5194/acp-15-11355-2015, 2015.

Lanz, V. A., Prévôt, A. S. H., Alfarra, M. R., Weimer, S., Mohr, C., Decarlo, P. F., Gianini, M. F. D., Hueglin, C., Schneider, J., Favez, O., D'Anna, B., George, C., and Baltensperger, U.: Characterization of aerosol chemical composition with aerosol mass spectrometry in Central Europe: An overview, Atmos. Chem. Phys., 10, 10453–10471, https://doi.org/10.5194/acp-10-10453-2010, 2010.

Mohr, C., DeCarlo, P. F., Heringa, M. F., Chirico, R., Slowik, J. G., Richter, R., Reche, C., Alastuey, A., Querol, X., Seco, R., Peñuelas, J., Jiḿenez, J. L., Crippa, M., Zimmermann, R., Baltensperger, U., and Prévôt, A. S. H.: Identification and quantification of organic aerosol from cooking and other sources in Barcelona using aerosol mass spectrometer data, Atmos. Chem. Phys., 12, 1649–1665, https://doi.org/10.5194/acp-12-1649-2012, 2012.

Ng, N. L., Herndon, S. C., Trimborn, A. M., Canagaratna, M. R., Croteau, P. L., Onasch, T. B., Sueper, D., Worsnop, D. R., Zhang, Q., Sun, Y. L., and Jayne, J. T.: An Aerosol Chemical Speciation Monitor (ACSM) for routine monitoring of the composition and mass concentrations of ambient aerosol, Aerosol Sci. Technol., 45, 780–794, https://doi.org/10.1080/02786826.2011.560211, 2011a.

Ng, N. L., Canagaratna, M. R., Jimenez, J. L., Zhang, Q., Ulbrich, I. M., and Worsnop, D. R.: Real-time methods for estimating organic component mass concentrations from aerosol mass spectrometer data, Environ. Sci. Technol., 45, 910–916, https://doi.org/10.1021/es102951k, 2011b.

Paglione, M., Gilardoni, S., Rinaldi, M., Decesari, S., Zanca, N., Sandrini, S., Giulianelli, L., Bacco, D., Ferrari, S., Poluzzi, V., Scotto, F., Trentini, A., Poulain, L., Herrmann, H., Wiedensohler, A., Canonaco, F., Prévôt, A. S. H., Massoli, P., Carbone, C., Facchini, M. C., and Fuzzi, S.: The impact of biomass burning and aqueous-phase processing on air quality: a multi-year source apportionment study in the Po Valley, Italy, Atmos. Chem. Phys. Discuss., 1–37, https://doi.org/10.5194/acp-2019-274, 2019.

Sage, A. M., Weitkamp, E. A., Robinson, A. L., and Donahue, N. M.: Evolving mass spectra of the oxidized component of organic aerosol: Results from aerosol mass spectrometer analyses of aged diesel emissions, Atmos. Chem. Phys., 8, 1139–1152, https://doi.org/10.5194/acp-8-1139-2008, 2008.

Stavroulas, I., Bougiatioti, A., Grivas, G., Paraskevopoulou, D., Tsagkaraki, M., Zarmpas, P., Liakakou, E., Gerasopoulos, E., and Mihalopoulos, N.: Sources and processes that control the submicron organic aerosol composition in an urban Mediterranean environment (Athens): A high temporal-resolution chemical composition measurement study, Atmos. Chem. Phys., 19, 901–919, https://doi.org/10.5194/acp-19-901-2019, 2019.

Stavroulas, I., Grivas, G., Liakakou, E., Kalkavouras, P., Bougiatioti, A., Kaskaoutis, D. G., Lianou, M., Papoutsidaki, K., Tsagkaraki, M., Zarmpas, P., Gerasopoulos, E., and Mihalopoulos, N.: Online chemical characterization and sources of submicron aerosol in the major mediterranean port city of piraeus, greece, Atmosphere (Basel)., 12, 1–28, https://doi.org/10.3390/atmos12121686, 2021.